International Journal of Solids and Structures xxx (2015) xxx–xxx

Contents lists available at ScienceDirect

International Journal of Solids and Structures

journal homepage: www.elsevier.com/locate/ijsolstr

Buckling-induced lock-up of a slender rod injected into a horizontal cylinder

J.T. Miller [a,1], T. Su [b], E.B. Dussan V. [b], J. Pabon [b], N. Wicks [b], K. Bertoldi [c,d], P.M. Reis [a,e,*]

[a] Dept. of Civil and Environmental Engineering, Massachusetts Institute of Technology, Cambridge, MA 02139, USA
[b] Schlumberger-Doll Research Center, One Hampshire Street, Cambridge, MA 02139, USA
[c] School of Engineering and Applied Sciences, Harvard University, Cambridge, MA 02138, USA
[d] Kavli Institute for Bionano Science and Technology, Harvard University, Cambridge, MA 02138, USA
[e] Dept. Mechanical Engineering, Massachusetts Institute of Technology, Cambridge, MA 02139, USA

ARTICLE INFO

Article history:
Received 10 April 2015
Received in revised form 19 June 2015
Available online xxxx

Keywords:
Mechanics of thin rods
Constrained buckling
Coiled-tubing
Wellbores
Experiments

ABSTRACT

We investigate the buckling and post-buckling behavior of an elastic rod injected into a horizontal, frictional, cylindrical constraint through experiments, numerical simulations, and scaling analyses. Particular emphasis is given to the onset of helical buckling which can lead to lock-up and prevent further injection. This problem is of timely importance to the petroleum industry due to the prevalence of Coiled Tubing (CT) technology in horizontal wells. An experiment is developed at the desktop scale to allow for a precise exploration of parameter space, including the important effects of radial clearance and natural curvature of the injected rod. In parallel, we perform computer simulations derived from first principles, implementing a dynamic Kirchhoff rod model that includes the frictional interaction between the rod and constraint. Our numerical simulations allow a direct comparison with experiments, as well as a systematic exploration of the parameter space. Moreover, a scaling analysis is performed to identify the key dimensionless parameter(s) that justifies using these findings at the field scale, thereby enabling the direct application of the results from our desktop experiments and numerical simulations to a problem of industrial relevance.

1. Introduction

Drilling methods for hydrocarbon production have evolved dramatically over the last century (Brusco et al., 2004), particularly with the development and adoption of *directional drilling* (drilling at an angle from vertical) during the second half of the twentieth century (Williams, 2004). This technology has been critical in enabling recent developments in the gas-shale market, especially in North America, by allowing for greater contact between the producing formation and the well (G.W.P. Council, 2009). As a result, horizontal drilling (well axis is within 10° of horizontal) now accounts for over half of the active wells being drilled in North America (Hughes, 2014). This ability to drill the well according to a specified trajectory has also led to the access of offshore fields from onshore sites worldwide (Bennetzen et al., 2010). By way of example, the recently drilled Z-42 Chayvo well in Russia set world records for both measured depth (12,700 m) and horizontal displacement (11,739 m) (Gupta et al., 2014).

After a horizontal well has been drilled and production has commenced, it may become necessary to access the entire length of the downhole environment for a variety of purposes, including cleaning out produced sand, acidizing (to remove near-wellbore damage), data logging, or mechanical actuation of valves (Acock et al., 2004; Afghoul et al., 1994). A device consisting of a single length of continuous, stainless steel tubing, called "Coiled Tubing" (CT), has been developed (ICoTA, 2005) for these intervention operations in horizontal wells which is more efficient and cost-effective than using the original drilling rig (see Fig. 1 for a representative example of a CT rig). The rig consists of a length of tubing spooled around a reel (hence, the origin of the name Coiled Tubing). For insertion into the wellbore, the tubing is passed through a guiding channel (often called a "gooseneck") and down through an injector head that pushes the tubing through the well head and into the well (underground).

The insertion of CT into horizontal sections can be challenging (Bhalla, 1995), because the CT lies at the bottom of the borehole,

* Corresponding author at: Dept. of Civil and Environmental Engineering and Dept. of Mechanical Engineering, 77 Massachusetts Av. #1-330, Massachusetts Institute of Technology, Cambridge, MA 02139, USA.
E-mail address: preis@mit.edu (P.M. Reis).
[1] Now a Research Associate with Schlumberger-Doll Research, One Hampshire Street, Cambridge, MA 02139, USA.

http://dx.doi.org/10.1016/j.ijsolstr.2015.07.025
0020-7683/

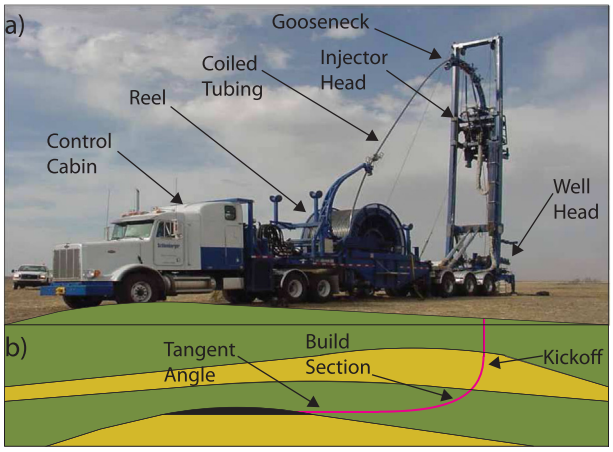

Fig. 1. (a) Photograph of a typical coiled tubing rig (Courtesy of Schlumberger-Doll Research). (b) Schematic representation of a horizontal well.

which leads to the development of frictional forces opposing insertion (resulting in a buildup of compressive axial load in the pipe in the horizontal section). After an initial, benign, sinusoidal buckling mode, the tubing undergoes localized helical buckling near the beginning of the horizontal section of the wellbore (Wicks et al., 2008). The helical configuration results in a rapidly increasing contact force between the pipe and the well wall, setting a limit to the amount of tubing that can be injected (sometimes also referred to as '*run in*') into a horizontal well, known as the *lock-up length* (Wicks et al., 2008). Currently, the lock-up length for Coiled Tubing is not sufficient to service all extended-reach wells.

This lock-up length is determined by geometry, material properties, and, to a lesser extent, the force available at the injector head to continue injecting Coiled Tubing. At the theoretical lock-up limit (when insertion force becomes unbounded and helical pitch decreases to zero), the maximum bending strains far surpass the ultimate yield strain of steel, which would cause the tubing to rupture. However, as shall be discussed further in Section 5.4, just after the initiation of helical buckling, maximum strains can be calculated with typical CT properties (Wicks et al., 2008; Lubinski and Althouse, 1962; Chen et al., 1990), and are approximately still an order of magnitude lower than the yield strain of a high-grade steel (Gere, 2006) and two orders of magnitude lower than that required for local buckling of the tubing (Brazier, 1927; Palmer and King, 2008). Up to the initiation of helical buckling, we can therefore consider the buckling process as an elastic problem, and is the primary regime of interest for this study.

Efforts to numerically simulate CT lock-up (van Adrichem and Newman, 1993; Bhalla, 1994), as well as discussions of mitigation techniques (Bhalla, 1995; Al-Dhufairi et al., 2010) can be found in the literature, although typically in a case-study format. There is, however, a timely need for a more predictive mechanical understanding of the problem to identify and explore the effect of the key physical parameters that control the buckling processes in order to explore novel reach extension technologies.

Here, we combine precision desktop experiments and numerical simulations to study the buckling of a slender rod injected into a horizontal cylindrical constraint. Our experiments permit precise control of the system geometry and injection speeds, as well as allow for direct measurement of the reaction force associated with injection. Our numerical simulations use an extensible, shearable Kirchhoff rod model to solve for the dynamics of the rod injected into the cylindrical constraint, subject to Coulombic friction. Excellent agreement is found between the two, with no fitting parameters. In both cases of experiments and numerical simulations, we focus on the elastic process of the initiation of helical buckling, with the aim of porting as much physical insight and understanding as possible to the field-scale problem. We also comment on the role of plasticity (not included in our framework) by quantifying the effect that the injection of a naturally curved rod has on horizontal reach.Finally, a scaling analysis is performed to identify the governing dimensionless parameters and allow for a substantiation of the relevance of our desktop-scaled experiments to the oilfield-scale problem.

Our paper is organized as follows. In Section 2, we begin by reviewing existing theoretical work. In Section 3, we present our desktop-scale experimental apparatus used to investigate the buckling of a cylindrically constrained rod. The parameter space is systematically studied, with an emphasis on the relative size of the cylindrical constraint, for both naturally straight and curved elastic rods. The simulation framework is presented next, Section 4, where particular care is taken for the contact model to accurately capture the frictional interaction between the rod and the surface of the horizontal constraint. The key dimensionless parameters of the system are identified through a scaling analysis done in Section 4.3. Results of our experiments and numerical simulations are directly compared in Section 5, first giving a direct comparison of injected length-reaction force curves (Section 5.1) before moving on to discuss the effect of radial clearance (Section 5.2) and the injected rod's natural curvature (Section 5.3) on the length of rod injected before helical buckling. Finally, we discuss our results in the field scale context with regards to plasticity and a broad exploration of dimensionless parameter space with our numerical simulations (Section 5.4) to confirm our scaling analysis of Section 4.3.

2. Review of existing literature

Coiled Tubing is typically manufactured in continuous lengths of up to 9 km, with outer diameters in the range of 2–10 cm (ICoTA, 2005). By contrast, drilling tubing is of similar length, but has larger diameters of ~12–20 cm (Wicks et al., 2008). Given the extreme slenderness of CT (and drillstrings), its behavior is well described in the framework of the mechanics of thin, inextensible and unshearable rods (Love, 1892; Audoly and Pomeau, 2010); an isotropic linear elastic constitutive description is assumed, and the primary nonlinearities that govern the mechanical behavior arise due to geometric effects. Next, we review a series of results from the literature that are relevant to our study, first for a fixed length of rod compressed inside a horizontal cylindrical constraint and then for a rod that is injected inside a horizontal pipe.

2.1. Axial loading of a fixed-length constrained rod

The buckling of a rod inside a cylindrical constraint was first studied within the context of drillstrings by Lubinski (1950), Lubinski and Althouse (1962), who identified both the sinusoidal and helical buckling modes of a fixed-length rod using equilibrium and energy methods. We shall refer to this fixed-length configuration as the *classic case*. An important distinction to make for this case is that axial load is assumed to be approximately constant along the length of the compressed rod, instead of the axially varying frictional loading discussed in the Introduction. Subsequent studies on this topic have mostly followed the assumptions of the compressed rod being initially straight, with a continuous and frictionless contact with the constraint.

When the constraint is horizontal, the critical axial load at which the rod transitions from the initially straight into a sinusoidal configuration is (Paslay and Bogy, 1964)

Please cite this article in press as: Miller, J.T., et al. Buckling-induced lock-up of a slender rod injected into a horizontal cylinder. Int. J. Solids Struct. (2015), http://dx.doi.org/10.1016/j.ijsolstr.2015.07.025

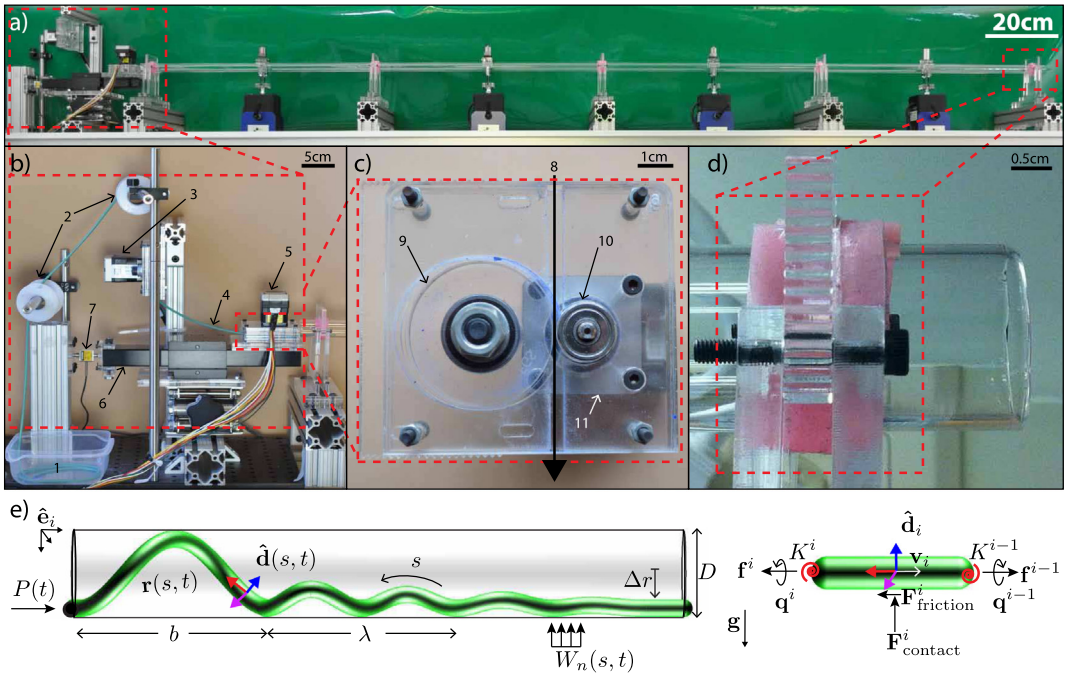

Fig. 2. (a) Side view of the experimental apparatus. The rod is injected from left to right. (b) Side view of the injection system. The elastic rod (1) is pulled over two feeder rollers (2), through a slave injector (3), forms a slack loop (4), and then is pulled through a primary injector (5) into the constraining glass cylinder. Reaction forces are transmitted over an air bearing slider (6) to the force sensor (7). (c) Bottom view of an injector. The rod is pulled through a channel (8) by an idler wheel (9) and a drive wheel (10) that is driven by a servo-stepper motor (11). (d) Close-up of an acrylic clamp holding the pipe in place. (e) Left, the rod configuration is defined by the centerline position $\mathbf{r}(s,t)$ and material frame triad $\hat{\mathbf{d}}$. At time t, the reaction force $P(t)$ can be measured at the injection point, and the relevant lengths include the helical pitch, b, sinusoidal wavelength, λ, and radial clearance, Δr. Right, discretized rod segment i with external contact and friction forces (which opposes the direction of velocity). The segment communicates internal forces and torques via a spring constant K.

$$P_s = 2\sqrt{\frac{EIw}{\Delta r}}, \tag{1}$$

where EI is the bending stiffness of the rod, w is its weight per unit length, and Δr is the radial clearance (see schematic in Fig. 2e). This result was derived following energy methods that take into account the gravitational potential of the rod, in addition to its bending strain energy and the work done by the external load, and assessing the stability of the straight configuration. Buckling is resisted by the combined effect of the bending stiffness of the rod and the cost in potential energy to lift its weight up the curvature of the constraining cylinder. The corresponding buckling wavelength, λ_s, at the onset of the sinusoidal configuration is (Dawson and Paslay, 1984)

$$\lambda_s = 2\pi\left(\frac{EI\Delta r}{w}\right)^{1/4}. \tag{2}$$

Further axial loading in the post-buckled regime results in the rod transitioning from a sinusoidal into a helical configuration. The load at which this transition occurs, P_h, is most commonly agreed to be (Chen et al., 1990)

$$P_h = \sqrt{2}P_s, \tag{3}$$

and the pitch of the resulting helix at onset is $b_h = \lambda_s/2^{1/4}$. Even though Eq. (3) is widely accepted in the literature for the prediction of P_h, there is some disagreement as to the $\sqrt{2}$ prefactor, with some authors arguing for values twice as large (Wu and Juvkam-Wold, 1993; Miska, 1995; Miska et al., 1996; Mitchell, 1997; Deli et al., 1998; Mitchell, 2002; Mitchell, 2008).

At even higher loads, $P_{h^+} > P_h$, the pitch of the helix decreases with load according to Lubinski and Althouse (1962)

$$P_{h^+} = \frac{8\pi^2 EI}{b_{h^+}^2}. \tag{4}$$

For a sinusoidally buckled rod, the normal contact force per unit length, W_n, has been found to not deviate significantly from the self-weight of the rod (Miska et al., 1996; Qiu, 1998). By contrast, after helical buckling, W_n increases quadratically with the axial load (Mitchell, 1986)

$$W_n = \frac{\Delta r P_{h^+}^2}{4EI}. \tag{5}$$

The effect of torsional loading on the critical buckling loads, P_s and P_h, has also been studied (Qiu, 1998; Deli et al., 1998). Gao and Miska (2009, 2010) examined the case of finite friction, and argued that amplification factors, ψ_c^s and ψ_c^h should be introduced in Eqs. (1) and (3), respectively, to account for an increased resistance to lateral buckling. In both studies, friction was assumed to act primarily in the *lateral* direction due to negligible axial velocities. These amplification factors have recently been found to improve the agreement between the predicted buckling loads of Eq. (3) and both experiments and numerical simulations (Miller et al., 2015). As will be discussed in Section 5.2, these amplification factors may be inappropriate for this study due to the presence of an axial velocity. Next, we review how the above results for the compression of a rod with fixed length have been adapted to the case of continuously injecting the rod into the cylindrical constraint, where axial loads arise due to the frictional rod-pipe contact.

2.2. Progressive injection of a rod into a constraint

Studies of progressively injecting a rod into a horizontal cylindrical constraint have emerged over the past decade, primarily in the context of CT operations in the oil and gas industry. We shall refer to this configuration of the problem as the *injection case*. The main focus of these investigations has been on characterizing the total length of rod, l_h, that can be inserted into the constraining

Please cite this article in press as: Miller, J.T., et al. Buckling-induced lock-up of a slender rod injected into a horizontal cylinder. Int. J. Solids Struct. (2015), http://dx.doi.org/10.1016/j.ijsolstr.2015.07.025

pipe before the initiation of the helical configuration and the subsequent *lock-up length*, at l_l, where the system jams.

Towards predicting both of these quantities, recent models by Wicks et al. (2008) and McCourt et al. (2002, 2004) have assumed that the axial load in the inserted rod that eventually leads to buckling arises from frictional resistance to the injection velocity, v, while neglecting the rod-constraint *lateral* friction. Similar to previous work outlined in Section 2.1, the injected rod was assumed to be inextensible, unshearable, and to remain in perfect contact with the constraint throughout the process. In order to predict critical length scales in the *injection case*, both groups assumed that Eqs. (1)–(5) remained applicable, despite violating some of the preconditions of these *classic case* results; namely the assumptions of negligible axial velocity, frictionless interaction, and constant axial load in the rod. As will be discussed in Section 5.2, non-negligible axial velocity will result in frictional resistance to injection that is directed primarily in the axial direction. This, in turn, leads to negligible resistance in the lateral direction, suggesting that there is not the need to consider the amplification factors ψ_c^s and ψ_c^h and bringing the analysis closer to the case with zero lateral friction. The applicability of the results reviewed in Section 2.1 for a rod with non-constant axial load as in the *injected case* is not as clear. Both groups assume the validity of Eq. (3) without formal rationale, although it could be argued that the axial load varies slightly over the length of a single helical pitch, which is the lengthscale of importance. As will be shown in Section 5, the predictions obtained from these *ad hoc* models perform well when compared against our experiments and numerical simulations. As such, porting the results from the *classic case* into the *injection case* appears to be appropriate.

In both of these studies, the injection velocity is considered to be the progenitor of axial frictional load, and inertial effects are neglected such that the process is treated as quasi-static. The contact force per unit length between the straight and sinusoidally buckled rod sections and the pipe is assumed to be the weight per unit length of the rod, i.e., $W_n = w$, such that prior to helical initiation, the injection force for a rod of length l is (Wicks et al., 2008; McCourt et al., 2004)

$$P = \mu w l. \tag{6}$$

This linear relationship is assumed to hold for $P \leqslant P_h$, where P_h is the critical helical buckling load defined in Eq. (3). Solving for l, provided that the injection force is equal to the critical helical buckling load (Wicks et al., 2008; McCourt et al., 2004), yields the length of rod at which helical initiation occurs

$$l_h = \frac{2\sqrt{2}}{\mu}\sqrt{\frac{EI}{w\Delta r}}. \tag{7}$$

For $l > l_h$, Eq. (6) is no longer valid and the contact force becomes nonlinear with the injection force according to Eq. (5). The injection force is then solved from Wicks et al. (2008), McCourt et al. (2004)

$$\frac{dP}{ds} = \mu W_n(s), \tag{8}$$

where s is the arc length along the rod's centerline, with $s = 0$ at the free tip. Eq. (8) assumes that the radial clearance is much smaller than the pitch of the helix ($\Delta r \ll b$), which is a valid assumption throughout this paper. Using Eq. (5) for W_n, P diverges at the finite injected length (Wicks et al., 2008; McCourt et al., 2004)

$$l_l = \frac{3\sqrt{2}}{\mu}\sqrt{\frac{EI}{w\Delta r}}, \tag{9}$$

which is referred to as the theoretical lock-up length. At lockup, the reaction load diverges and the helical pitch length tends to zero.

McCourt et al. (2002), McCourt et al. (2004) conducted the only laboratory-scale experiments in the existing literature, where they monitored the injection load during insertion and found good agreement with their predictions. In these tests, the rod-glass dynamic friction coefficient was treated as a fitting parameter, which was found to lie in the range $0.6 \leqslant \mu \leq 1.2$. When translating the results to the field scale, they used the aspect ratio between the diameters of the rod and constraint as the primary geometric scaling factor, an alternative to which we shall provide in 4.3.

Finally, referring back to the photograph of a typical CT unit shown in Fig. 1, one can see that the Coiled Tubing is spooled. This spooling does plastify (i.e., deforms irreversibly) the steel pipe, thereby imparting a natural curvature, κ_n (Newman and Newburn, 1991; Bhalla, 1994). Even though CT rigs sometimes include a *pipe straightener*, especially in operations where maximizing horizontal reach extension is a priority, the tubing still exits the injector head into the wellbore with a finite value of residual curvature in the range $0.1 < \kappa_n[\mathrm{m}^{-1}] < 0.26$ (Zheng and Sarmad, 2005; Bhalla, 1995). Zheng and Sarmad (2005) considered the effect of κ_n on l_l, assuming that the rod adopted a helical shape throughout injection, and proposed

$$l_l = \frac{P_h}{\mu w} + \frac{2}{\mu\kappa_n}\ln\left(1 + \frac{2EI\kappa_n}{\Delta r P_h}\right), \tag{10}$$

where P_h was provided in Eq. (3) and all other parameters have also been defined above. In the case of a naturally straight rod ($\kappa_n = 0$), Eq. (10) recovers Eq. (9). To date, Eq. (10) has not yet been compared against experimental results. Eq. (10) predicts a decrease in l_l with increasing κ_n, and field-scale tests have indeed confirmed that straightening CT prior to insertion helps extend the maximum reach before lock-up occurs (Bhalla, 1995).

3. Experimental methods

We now introduce the experimental apparatus and protocol used to explore and characterize the buckling progression of a rod injected into a cylindrical constraint. The prominence of geometric instead of material nonlinearities in this problem makes it a good candidate for a systematic mechanical investigation at the desktop scale. Still note that the scaling is not one-to-one, as we shall see in more detail in Section 4.3. There are a number of advantages in focusing on precision model experiments instead of direct field-scale testing. These include a greater flexibility to systematically explore a wide range of the parameter space, the ability to directly visualize progression of tests, precise control over the governing parameters, and the relative low cost of the experimental tests.

3.1. Apparatus

In Fig. 2a we present a photograph of our experimental apparatus, which comprises an injection system and a horizontal pipe that was mounted onto a custom-built rigid aluminum frame by five equally spaced acrylic clamps (detailed photograph in Fig. 2d). The constraining pipe was made out of borosilicate glass with total length of $L = 2.46$ m. The inner diameter of the pipe was varied (8 values) in the range $6.6 < D[\mathrm{mm}] < 33.6$.

The rod injection system (detailed photograph in Fig. 2b) was located on one of the extremities of the pipe, and its vertical position was adjustable to allow for the rod to be injected in contact with the bottom surface of the constraining pipe. The injection speed was controlled in the range $0 < v[\mathrm{cm/s}] < 20$. In parallel during each test, the reaction force was recorded using a 4.5-N-capacity load cell (0.01-N resolution, taking into account system losses, as described below). This injection force, P, could

Please cite this article in press as: Miller, J.T., et al. Buckling-induced lock-up of a slender rod injected into a horizontal cylinder. Int. J. Solids Struct. (2015), http://dx.doi.org/10.1016/j.ijsolstr.2015.07.025

therefore be expressed as a function of elapsed time, t, or injected rod length, $l = vt$. During injection, a set length of excess rod was temporarily spooled in a plastic container (lower left corner of Fig. 2b), brought over two feeder rollers, and fed first through the slave injector and then the master injector. A small segment of rod (referred to as the *slack loop*) was suspended between the slave injector and the master injector, and then injected into the constraining glass pipe.

The injection force was transmitted from the master injector into the load cell, across a horizontal linear air bearing to minimize frictional resistance. The load cell measured the sum of the reaction force, the tension in the rod fed into the master injector, and the frictional losses of the air bearing. The air bearing exhibited low frictional losses (<0.01 N), and the slack loop provided a constant tension (measured before each test) that could be balanced out of the recorded force signal from a control test.

The slave and master injectors were aligned perpendicularly but were identical in design, which was modified from the Makerbot Cupcake filament drive mechanism (MakerBot, 2013) (see Fig. 2c). For each injector, the rod was inserted into a channel that was sandwiched between acrylic plates, then gripped between an idler and drive wheel. Injection was activated by rotating the drive wheel at a set speed using a computer-controlled stepper motor, while the idler wheel was free to rotate. The grip of the two wheels prevented the rod from slipping or twisting at either injector. Calibration of the two injectors ensured identical operating speeds, and hence a constant-tension slack loop.

During each test, the injection load signal was digitized at 1 kHz and synchronized (to within 0.02 s) to a digital video camera. The camera recorded the top view of the (transparent) constraining pipe in the 30 cm neighborhood of the injector at 59.94 frames per second. A more detailed account of the experimental apparatus can be found in Miller (2014).

3.2. Fabrication of the rods

The elastic rods employed in the experiments were custom-fabricated using an injection molding procedure out of vinyl polysiloxane (VPS, Zhermack Elite Double 32). This two-part silicone-based rubber can be cast to provide control over the material and geometric properties, including the natural curvature.

The two-part VPS polymer was injected into a polyvinyl chloride (PVC) tube (inner diameter, $D_i = 3.16$ mm, and outer diameter, $D_o = 5.00$ mm) that was laid straight along a rigid track. The system was allowed to set for at least one hour to ensure full curing and the PVC tubing was then cut to release the inner VPS elastic rod. The diameter of the resulting rod was set by the inner diameter of the PVC tubing; $d = 3.16 \pm 0.05$ mm. Rods manufactured with this process were naturally straight (i.e., $\kappa_n = 0$), and were used for all results presented except those in Section 5.3. The Young's modulus of the elastomer was measured to be $E = 1290 \pm 12$ kPa, the Poisson ratio was $\nu \approx 0.5$, and the volumetric mass was $\rho = 1210 \pm 8$ kg/m^3.

To fabricate rods *with* natural curvature, the PVC tubes were first wound around a cylindrical object of diameter, D_m, after which the molding process was similar to that described above. Upon curing, the natural curvature of the resulting elastomeric rod was $\kappa_n = 2/(D_o + D_m)$ and varied in the range $0 < \kappa_n[\mathrm{m}^{-1}] < 65$. More information regarding this technique can be found in Lazarus et al. (2013), Lazarus et al. (2013), Miller et al. (2014), Jawed et al. (2014).

Particular care was taken to condition the surface of the rod, in order to ensure a frictional rod-constraint interaction that was both homogeneous along the arc length and reproducible across multiple tests. The rod was coated with loose chalk powder (Irwin brand chalk for snap-lines, primarily composed of calcium carbonate) and excess chalk was then wiped off with a cloth by applying a constant normal pressure while moving it across the full length of the rod. Moreover, the inner surface of the constraining pipe was cleaned prior to each series of tests by pulling a cotton cloth through the pipe to remove any chalk that may have been deposited in the previous test.

This protocol resulted in a consistently repeatable coefficient of dynamic friction that was measured to be $\mu = 0.54 \pm 0.11$ across all injection speeds and constraining pipes. From now on, we shall assume a dry Coulomb frictional interaction between rod and pipe.

3.3. Protocol for the experimental tests

Each experimental run comprised the following sequence of steps: (i) cleaning the pipe; (ii) conditioning the rod; (iii) preparing the injection subsystem; (iv) injecting the rod; and finally (v) withdrawing the rod. A single test included repeating steps (iv) and (v) 10 times for statistical purposes. Prior to the injection stage step, the tension in the slack loop was recorded for approximately 5 s to allow for a balancing of the injection reaction, and the digital video camera was switched on to later synchronize the reaction force signal and the recorded video. Data from both the load cell and the video camera were also acquired during the withdrawal stage. After the series of 10 experimental runs (a test) was concluded, the rod was removed from the injection subsystem for cleaning, and the constraining pipe was replaced for a different clearance, if desired.

4. Modeling and simulation methods

Our modeling approach is based on Kirchhoff's description of a thin elastic rod that includes the constraint (Section 4.1). This model forms the basis of the numerical simulations that we have developed (Section 4.2). The Kirchhoff rod model is also used for a scaling analysis (Section 4.3) that identifies the primary dimensionless parameters of the system and allows for an interpretation of our desktop-scale experimental results, in the context of the original application of lock-up of CT, at the field scale.

4.1. Kirchhoff rod inside a cylindrical constraint

The mechanics of a thin elastic rod are often described using Kirchhoff's model (Love, 1892; Kirchhoff, 1859; Clebsch et al., 1862; Maddocks, 1984; Antman, 2005), which has the ability to capture geometric nonlinearities, dynamics, and the presence of natural curvature (Goriely and Tabor, 1998; Goyal et al., 2008). We use a shearable and extensible version of Kirchhoff's model (Shi and Hearst, 1994) and assume a linearly elastic material constitutive relation.

A Kirchhoff rod is characterized by both its centerline position, $\mathbf{r}(s,t)$, and a material triad, $\hat{\mathbf{d}}_i(s,t)$ $(i = 1,2,3)$, attached to every cross section that follows the twist along the rod (schematic in Fig. 2e). Both $\hat{\mathbf{d}}_1$ and $\hat{\mathbf{d}}_2$ lie on the cross section plane, whose unit normal is $\hat{\mathbf{d}}_3$, and the parameterization is done as a function of the *undeformed* rod arc length coordinate, s, with the free end of the rod located at $s = 0$. The dynamics are captured by the velocity of the centerline, $\mathbf{v}(s,t)$, and the angular velocity of the material frame, $\boldsymbol{\omega}(s,t)$, both defined relative to the global inertial frame, $\hat{\mathbf{e}}_i$ $(i = 1,2,3)$. The global frame is assumed to have its origin at the bottom tangent of the pipe at the injection site such that $\hat{\mathbf{e}}_1$ is oriented along the pipe's long axis. The bending and twisting strains, $\boldsymbol{\kappa}(s,t)$ (with $\kappa_3 = \boldsymbol{\kappa} \cdot \hat{\mathbf{d}}_3$ denoting the twisting strain), can be

Please cite this article in press as: Miller, J.T., et al. Buckling-induced lock-up of a slender rod injected into a horizontal cylinder. Int. J. Solids Struct. (2015), http://dx.doi.org/10.1016/j.ijsolstr.2015.07.025

obtained from $\hat{\mathbf{d}}_i' = \boldsymbol{\kappa} \times \hat{\mathbf{d}}_i$. Throughout, prime represents differentiation with respect to arc-length, *e.g.*, $\mathbf{r}' = \partial \mathbf{r}/\partial s$, and dotted quantities are differentiated with respect to time, *e.g.*, $\dot{\mathbf{r}} = \partial \mathbf{r}/\partial t$. Note that $\hat{\mathbf{d}}_3$ is not necessarily tangent to the centerline given that tensile and shear strains, $\boldsymbol{\gamma}(s,t) = \mathbf{r}' - \hat{\mathbf{d}}_3$ (with $\gamma_3 = \boldsymbol{\gamma} \cdot \hat{\mathbf{d}}_3$ representing tensile strain), can be non-zero.

The internal forces, $\mathbf{f}(s,t)$, are related to the strains through linear elasticity, such that $\mathbf{f}(s,t) = \mathbf{B}\boldsymbol{\gamma}(s,t)$, where $\mathbf{B} = \mathrm{diag}(GA, GA, EA)$ in the local $\hat{\mathbf{d}}_i$ frame and G and A are the shear modulus and cross-sectional area of the rod, respectively. Similarly, the internal moments, $\mathbf{q}(s,t)$, are related to bending strains through $\mathbf{q}(s,t) = \mathbf{G}\boldsymbol{\kappa}(s,t)$, where $\mathbf{G} = \mathrm{diag}(EI, EI, GJ)$ in the local $\hat{\mathbf{d}}_i$ frame and I and J are the second moment of inertia and polar moment of inertia of the rod, respectively.

The dynamics of the rod are then described in the non-inertial reference frame $\hat{\mathbf{d}}_i$ through the conservation of linear and angular momentum, respectively,

$$(m\dot{\mathbf{v}}) + \boldsymbol{\omega} \times (m\mathbf{v}) = \mathbf{f}' + \boldsymbol{\kappa} \times \mathbf{f} + mg\hat{\mathbf{e}}_3 + \mathbf{F}_{\text{contact}} + \mathbf{F}_{\text{friction}}, \tag{11}$$

and

$$\left(\mathbf{I}\dot{\boldsymbol{\omega}}\right) + \boldsymbol{\omega} \times (\mathbf{I}\boldsymbol{\omega}) = \mathbf{q}' + \boldsymbol{\kappa} \times \mathbf{q} + \left(\boldsymbol{\gamma} + \hat{\mathbf{d}}_3\right) \times \mathbf{f} + \mathbf{Q}_{\text{ext}}, \tag{12}$$

where $m = \rho A$ is the linear density of the rod of volumetric density ρ and cross-sectional area A, and $\mathbf{I}$ is its mass moment of inertia. The normal contact force between the constraining pipe and rod at points of contact per unit rod reference length is represented by $\mathbf{F}_{\text{contact}}$, $\mathbf{F}_{\text{friction}}$ is the friction exerted by the constraint on the rod (per reference length), and $\mathbf{Q}_{\text{ext}}$ is the externally applied moment (also per unit rod reference length). The forms of $\mathbf{F}_{\text{contact}}$, $\mathbf{F}_{\text{friction}}$, and $\mathbf{Q}_{\text{ext}}$ are specific to our case of injecting a rod into a cylindrical constraint and are discussed in more detail below.

For the boundary conditions, we assume that the strains at the free end ($s = 0$) vanish,

$$\boldsymbol{\gamma}(0,t) = \mathbf{0}, \quad \boldsymbol{\kappa}(0,t) = \mathbf{0}. \tag{13}$$

We also assume that, at the injector ($s = vt$), the rod is injected at the velocity, v, parallel to the axis of the constraining pipe with zero angular velocity,

$$\mathbf{v}(vt,t) = v\hat{\mathbf{e}}_1, \quad \boldsymbol{\omega}(vt,t) = \mathbf{0}. \tag{14}$$

Returning to the conservation of linear momentum, Eq. (11), we now discuss the external forces, $\mathbf{F}_{\text{contact}}$ and $\mathbf{F}_{\text{friction}}$, in more detail. Firstly, the normal contact force is in the radial direction of the constraint when rod-channel contact occurs. It consists of an elastic and an inelastic part,

$$\mathbf{F}_{\text{contact}} = -(N_{\text{elastic}} + N_{\text{inelastic}})\hat{\mathbf{n}}. \tag{15}$$

The magnitude of the elastic contact force per unit length N_{elastic} can be determined by the radial penetration δ of the rod into the constraint (if penetration occurs)

$$\delta = BN_{\text{elastic}}\left[\frac{2}{3} + \log\left(\frac{\Delta r}{BN_{\text{elastic}}}\right)\right] + \frac{N_{\text{elastic}}}{k}, \tag{16}$$

where B and k are two constants computed using the geometry of the rod and the constraint, and Δr is the radial clearance of the rod inside the constraint. On the other hand, the magnitude of the inelastic part of the contact force $N_{\text{inelastic}}$ is determined by the radial velocity of the rod v_n at the point of contact,

$$N_{\text{inelastic}} = Cv_n, \tag{17}$$

where C is a constant computed using the coefficient of restitution of the contact. Both the elastic and inelastic parts of the contact force act normal to the inner surface of the constraining pipe if, and only if, it is in contact with the pipe wall. For more information of the contact model, we refer the readers to Roark and Young (1975), Pabon et al. (2009), Pabon et al. (2010), Pabon et al. (2011).

Segments of the rod in contact with the constraint result in a frictional interaction modeled as a Coulomb friction that opposes the direction of motion of the rod

$$\mathbf{F}_{\text{friction}} \leqslant -\mu|\mathbf{F}_{\text{contact}}|\frac{\mathbf{v}}{|\mathbf{v}|}. \tag{18}$$

In our simulations, we do differentiate between static and dynamic values of μ. The numerical implementation of Eq. (18) will be discussed in detail in Section 4.2, but at this stage, it is important to note that friction is modeled as acting on the surface of the rod, a distance r from its centerline. When $\mathbf{F}_{\text{contact}} \cdot \hat{\mathbf{d}}_3 \neq 0$, this results in an external torque

$$\mathbf{Q}_{\text{ext}} = r\hat{\mathbf{n}} \times \mathbf{F}_{\text{friction}}. \tag{19}$$

that must be considered in Eq. (12) for the balance of angular momentum. Note that for the purposes of the scaling we shall discuss in Section 4.3, we do not differentiate between static and dynamic coefficients of friction, using only one value.

4.2. Numerical procedure

In our numerical simulations, we solve for the dynamics of an elastic rod being injected into a cylindrical constraint, following the approach that has been successfully applied to the transient dynamics of drillstrings (Pabon et al., 2009; Pabon et al., 2011). First, the rod is discretized into segments, each of which is characterized by its position and orientation, $\mathbf{r}_i$ and $\hat{\mathbf{d}}_i$, respectively (see schematic in Fig. 2e). Extra segments are added at the injection point with a velocity that is imposed at these new elements.

At each computational time step, strains (including extension, bending, twisting, and shear strains) for each segment are computed using the current position and orientation of the rod following the Kirchhoff model described above. The stresses along the rod are computed from these strains, making use of an isotropic linear elastic constitutive law (justified by small material strains despite large displacements and rotations). From these stresses, we calculate the internal forces acting between adjacent segments that, combined with the external forces (*e.g.*, gravity and the normal/-tangential frictional contact forces with the constraint), yield the total force on each segment. The acceleration of the segments can then be determined, allowing for rod configuration and orientation to be updated in the subsequent time-step. Buckling would not occur in the simulation if the rod were perfectly straight. To correct for this, a small lateral perturbation force is applied on randomly selected segments at each computational step. The magnitude of this perturbation force decreases exponentially as time increases.

The friction force is applied on the surface of the rod instead of on its centerline. Therefore, it can lead to an external moment on the rod centerline. Moreover, in each computational time step, we ensure that the friction force is always dissipative. We account for both static and dynamic coefficients of friction (measured experimentally), and have the capability to simulate cases where friction in the axial and transverse directions are not equal. In all cases discussed in this paper, however, the friction coefficient is set to be isotropic.

Finally, a Newton–Raphson iteration scheme is used to integrate the equations of motion and update the rod configurations. The time step in the simulation is chosen to be smaller than (usually 90% of) the time for an elastic axial wave to travel through one discrete segment. The segment length was tailored for different radial clearances based on convergence analyses.

Please cite this article in press as: Miller, J.T., et al. Buckling-induced lock-up of a slender rod injected into a horizontal cylinder. Int. J. Solids Struct. (2015), http://dx.doi.org/10.1016/j.ijsolstr.2015.07.025

4.3. Scaling analysis

To establish a quantitative connection between the results from our precision desktop-scale experiments and the field-scale problem, we now turn to a dimensional analysis of Eqs. (11), (12) and (15)–(19) towards identifying the relevant scaling factors. We first simplify our contact force model, replacing Eq. (15) with a linear contact force-penetration relationship,

$$\mathbf{F}_{\text{contact}} = \begin{cases} \mathbf{0} & (\text{if } R < \Delta r), \\ -k(R-\Delta r)\hat{\mathbf{n}} & (\text{if } R \geqslant \Delta r), \end{cases} \tag{20}$$

where $\hat{\mathbf{n}}$ is the unit normal vector on the constraint surface, R is the radial displacement of the rod from the centerline of the constraint, and k is a linear spring constant. This simplification of the contact force is performed to reduce the number of unknown parameters, while retaining the interaction between rod and constraint as a fundamental ingredient of the problem.

Our description then involves nine independent variables – r, ρ, E, G, Δr, k, μ, ν,, and g – with three dimensional units – [kg], [m], and [s]. We now assume, for simplicity, that the static and dynamic coefficients of friction are both equal to μ. The Buckingham Π theorem (Buckingham, 1914) establishes six independent dimensionless parameters that are listed in Table 1. In this non-dimensionalization procedure, we have taken the sinusoidal buckling wavelength, λ, as defined in Eq. (2), and the speed of sound of the rod, $v_{\text{sound}} \equiv \sqrt{E/\rho}$, to be the characteristic physical length and velocity scales, respectively. The equations of motion of the rod can thereby be readily rewritten in dimensionless form using the parameters in Table 1. For the sake of simplicity, we instead now follow a scaling approach that will be supported by the numerical results in Section 5.4. We start by determining the dominant dimensionless parameter in Table 1. In both the laboratory and the field cases, the constraint stiffness, ϕ, and the ratio between inertial and elastic effects, η, are small, with $\eta \to 0$ and $\phi \approx 10^{-4} - 10^{-5}$, and can be ignored in our analysis. Moreover, the Poisson's ratio is only found to vary over a narrow range, $0.3 < \nu < 0.5$, for typical engineering materials such that it can also be neglected in this scaling comparison. This leaves three dimensionless parameters to be considered. The first is a measure of the rod slenderness, ξ_r, which can be used to compare strains between the laboratory and field cases by recognizing that the sinusoidal buckling strain, ϵ_s, of a cylindrically constrained fixed length of rod (Paslay and Bogy, 1964) can be directly related to our dimensionless parameters through $\epsilon_s = 2\pi^2\xi_r^2$. This reinforces the fact that material strains are low ($< 1\%$) at the onset of buckling, with geometric nonlinearities giving rise to the large deformations of the rod.

Recalling from Section 1 that we are primarily interested in exploring the length of injected rod for helix initiation, l_h, which ensures that we remain in the elastic regime of the problem (discussed in further detail in Section 5.4), the remaining dimensionless parameters can be combined to rewrite Eq. (7) as

$$\frac{l_h}{\lambda} = \frac{\sqrt{2}}{2\pi^2}\frac{1}{\mu\xi_{\Delta r}}. \tag{21}$$

Therefore, a relevant comparison between the results at the laboratory and field scales requires matching μ and $\xi_{\Delta r}$. Given that friction is highly dependent on the specific field conditions and also typically lies in a narrow range (similar to our statement on ν, above), we opt to compare $\xi_{\Delta r}$. In the field, this parameter lies in the range $0.002 \lesssim \xi_{\Delta r} \lesssim 0.003$, whereas in our experiments we have $0.015 \leqslant \xi_{\Delta r} \leqslant 0.076$. Typically, there is therefore at least an order of magnitude difference for $\xi_{\Delta r}$ between the field and the laboratory. Beyond the lack of an exact overlap in $\xi_{\Delta r}$ between the two cases, there are other factors that also preclude a direct emulation and matching of the field scenario in the laboratory, in particular the exact geometry of boreholes in the field (including vertical sections and doglegs). Still, we conjecture that the same physical processes are at play in the two cases. A quantitative support for this assertion will be provided in Section 5.4 where we shall use the numerical simulations (once they have been validated against experiments) to show that Eq. (21) holds in the full range $0.001 < \xi_{\Delta r} < 0.8$ that encompasses the laboratory and the field cases.

Table 1
List of dimensionless parameters constructed from the dimensional quantities in Eqs. (11) and (12).

Parameter	Definition
Coefficient of Friction	μ
Poisson's Ratio	$\nu = E/(2G) - 1$
Constraint Stiffness	$\phi = \rho g/(k\Delta r)$
Inertia vs. Elasticity	$\eta = v/v_{\text{sound}}$
Rod Slenderness	$\xi_r = r/\lambda$
Constraint Slenderness	$\xi_{\Delta r} = \Delta r/\lambda$

5. Results

5.1. Phenomenology

In Fig. 3a, we show representative photographs of the rod near the injector during a typical test, as the rod is progressively inserted into the horizontal cylindrical constraint ($D = 12.0$ mm, $\Delta r = 4.42$ mm, $v = 0.1$ m/s). During the test, we record the reaction force at the injector, P, as a function of the injected length of rod, l, which is plotted in Fig. 3b for the experimental run (filled circles) and the corresponding simulation (open circles).

During the early stages of the injection process (*e.g.*, Fig. 3a,i, $l = 0.22$ m), the rod lies in a straight configuration along the bottom surface of the constraining pipe since frictional forces are not yet sufficiently large to induce buckling. During this regime, there is an approximately linear relationship between l and P. Upon further injection, however, a sinusoidal buckling mode is observed near the injector, where the rod climbs up alternate sides of the pipe (Fig. 3a,ii, $l = 0.73$ m). This buckling mode is localized near the injector and the rod is straight near the tip; the configuration of the rod is spatially heterogeneous. Still, immediately after this transition, there is not an appreciable change in the relation between P and l. As the test progresses, the amplitude of the sinusoidal segment increases, until portions of the rod reach approximately halfway up the constraining pipe. At this stage, a helically buckled configuration emerges near the injector (Fig. 3a,iii, $l = 0.79$ m). We shall refer to the moment when the rod first contacts the top of the constraining pipe as the *helical initiation*. The total arc length of injected rod at helical initiation is denoted as l_h (solid vertical line in Fig. 3b). Past helical initiation, P increases rapidly (and nonlinearly) with increasing l, as new pitches form on the helical portion that hamper injection. The locally periodic structure in the $P - l$ signal for $l > l_h$ corresponds to the formation of new helical pitches. The pitch length decreases while P increases in a way consistent with Eq. (4) for the fixed-length case. Eventually, lock-up occurs once the pitch size approaches the rod diameter, and the rod self-contacts in a region close to the injector, such that the pitch angle there becomes approximately perpendicular to the axial direction of the constraint (see region highlighted by the dashed oval in Fig. 3a,iv). Beyond this point, no further injection is possible due to jamming and injection is stopped (Fig. 3a,iv, $l = 0.98$ m).

In Fig. 3b we superpose the P–l signal for experiments and simulations with l_h indicated with vertical lines (solid and dashed,

Please cite this article in press as: Miller, J.T., et al. Buckling-induced lock-up of a slender rod injected into a horizontal cylinder. Int. J. Solids Struct. (2015), http://dx.doi.org/10.1016/j.ijsolstr.2015.07.025

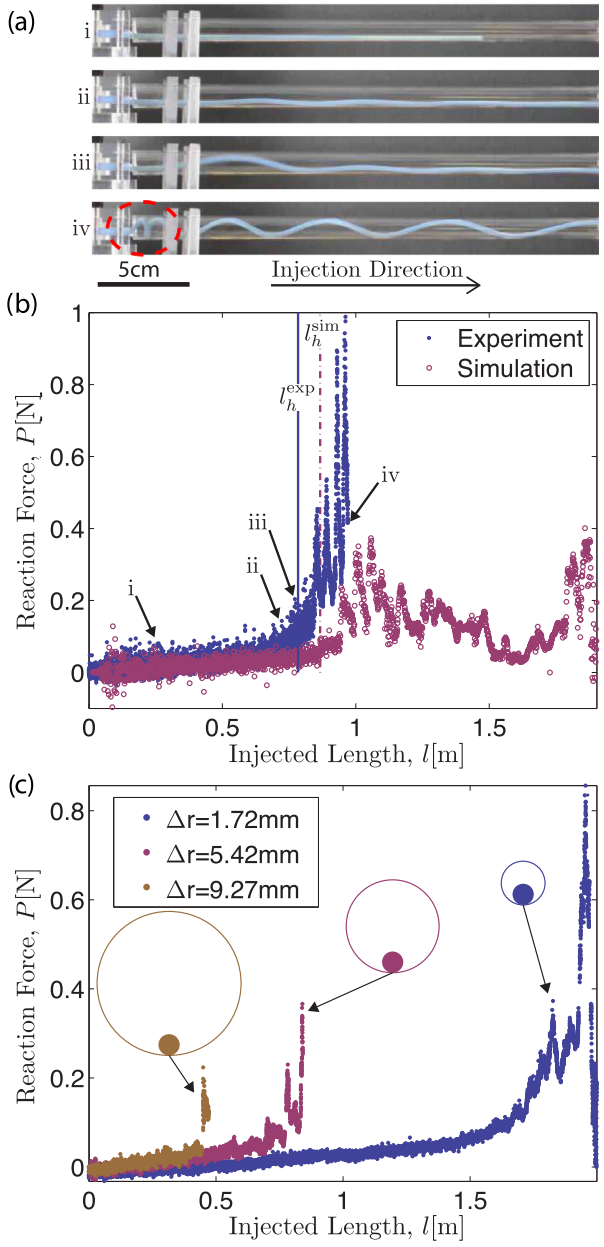

Fig. 3. (a) Side-view photographs of rod configurations for a rod injected into a constraining pipe with $D = 12.0$ mm at $v = 0.1$ m/s: (i) purely straight, (ii) sinusoidally buckled, (iii) helical initiation, and (iv) lock-up (note the near vertical pitch angle inside the region highlighted by the dashed red oval). (b) Reaction force at the injector as a function of injected length for the run in (a) for experiments (solid circles) and simulations (hollow circles). (c) Reaction force vs. l for three different sized cylindrical constraints with radial clearances of $\Delta r = 1.72, 5.42$, and 9.27 mm. (For interpretation of the references to colour in this figure legend, the reader is referred to the web version of this article.)

respectively). Both signals terminate at lock-up. In the experiments, lock-up is defined by the moment when injection ceases (the tip of the rod stops moving). In the simulation, lock-up is defined by the onset of self-contact in the helical region of the rod. Good agreement is found between the two, with helical initiation lengths at $l_h^{exp} \approx 0.55$ m for the experiments and $l_h^{sim} = 0.7$ m for the simulations. However, lock-up in the simulations ($l_l^{sim} \approx 1.75$ m) occurs significantly later than in the experiments ($l_l^{exp} \approx 0.75$ m). After l_h, a greater amount of helix rearrangement and collapse of helical pitches away from the injector was observed in simulations than in experimental runs, possibly due to the fact that material damping was not included in our simulations. A material model including damping was not implemented to avoid specificity, i.e. rubber and steel exhibit different damping behavior. However, the fact that we observe high strain rates (of the order of $0.1\,s^{-1}$) in the numerically simulated rod near the injector between helix initiation and lockup (the region of disagreement between our experiments and simulations) indicates that material damping may lead to non-negligible effects during the lockup process. Furthermore, high strain values (on the order of 3%) in the simulated rod near the experimentally observed lockup lengths suggests that our linear elastic assumption may no longer be valid beyond l_h. We speculate that a combination of these two factors is the cause of the discrepancy in l_l between the two methods.

Thus far, we have focused on results for $\Delta r = 4.42$ mm (diameter of the constraint was $D = 12.0$ mm). Similar behavior was observed for all other radial clearances explored. In Fig. 3c, we plot the experimental reaction force as a function of injected length for three other radial clearances ($\Delta r = 1.72, 5.42$, and 9.27 mm). The same sequence of configurations (straight, sinusoidal, helical, lock-up) was observed for all clearances. However, the lock-up length increases with decreasing Δr, which is discussed next.

5.2. Effect of radial clearance

We now investigate the effect of radial clearance on the total length of rod that can be injected prior to helical initiation, which is a precursor of lock-up. The primary focus is to compare our experimental and numerical results against one another and the existing theories reviewed in Section 2. All quantities are made dimensionless according to the parameters presented in Table 1 that resulted from our scaling analysis in Section 4.3.

In Fig. 4, we present the dependence of the dimensionless helix initiation length, $\bar{l}_h = l_h/\lambda$ as a function of dimensionless radial clearance, $\xi_{\Delta r} = \Delta r/\lambda$, for a rod injected at $v = 0.1$ m/s into constraining pipes over a range of diameters. Both $\bar{l}_h$ and $\xi_{\Delta r}$ have been normalized by the sinusoidal buckling wavelength defined in Eq. (2). Good agreement is found between experiments (filled symbols), numerics (open symbols) and the theoretical prediction (solid line) of Eq. (21). The theoretical prediction includes an envelope (in between the two dashed lines) that accounts for the experimental uncertainty in the dynamic friction coefficient, $\mu = 0.54 \pm 0.11$, that was measured independently (see Section 3.2). We confirm that helical initiation is delayed for tighter clearances according to $\bar{l}_h \sim 1/\xi_{\Delta r}$, and this result also serves as the validation of our numeric simulations.

As a general trend in Fig. 4, the numerical results are consistently above the experimental results by $\sim 20\%$, which in turn are generally in better agreement with Eq. (21). This small but systematic discrepancy between simulations and experiments can be attributed to the presence of imperfections in the fabricated rods, which lower the critical buckling load that is directly related to injected length through Eq. (6) (Timoshenko et al., 1961). On the other hand, the derivation of Eq. (21) assumed a naturally straight injected rod (without imperfection) but did not consider any lateral frictional effects. This may account for the fact that the predicted values are lower than the numerical results, and coincidentally closer to the experiments.

The good agreement that we have found between Eq. (21) and both the experimental and numerical results was, *a priori*, not to be expected. In order to arrive to this prediction, the results from Section 2.1 – which assumed constant axial load, negligible axial velocity, and frictionless contact – were applied in an *ad hoc* manner to the problem at hand. However, the axial velocity that ensues from injection implies that friction acts predominantly in the axial

Please cite this article in press as: Miller, J.T., et al. Buckling-induced lock-up of a slender rod injected into a horizontal cylinder. Int. J. Solids Struct. (2015), http://dx.doi.org/10.1016/j.ijsolstr.2015.07.025

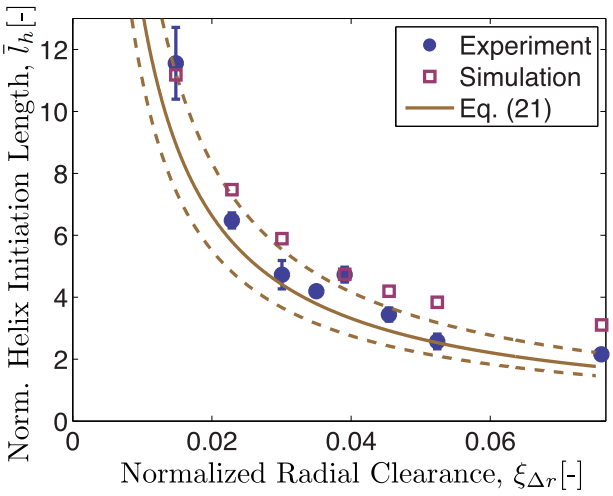

Fig. 4. Normalized helix initiation length as a function of normalized radial clearance for experiments (solid circles with error bars), simulations (hollow squares), and theoretical predictions (lines – Eq. (21)). Theoretical predictions and simulations use the experimentally measured dynamic friction coefficient $\mu = 0.54 \pm 0.11$.

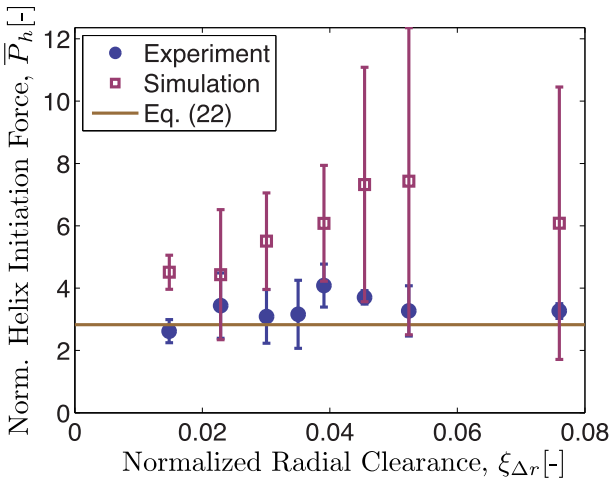

Fig. 5. Normalized reaction force at the injector at $l_h, \bar{P}_h$, as a function of $\xi_{\Delta r}$, for experiments (solid points), simulations (hollow squares), and theoretical predictions (solid line) from Eq. (22).

direction (provided that the injection speed is greater than the local, lateral velocities of the reconfiguration due to buckling), making frictional resistance to lateral motion negligible. Furthermore, as discussed in Section 4.3, the axial velocities are well below the speed of sound in the injected rod, which supports that fact that inertial effects can still be neglected.

Turning to the injection load at the onset of helix initiation, P_h, i.e., when $l = l_h$ in Eq. (6), we first make it dimensionless,

$$\bar{P}_h = P_h \sqrt{\frac{\Delta r}{EIw}} = 2\sqrt{2}, \tag{22}$$

and find that it is expected to be independent of $\xi_{\Delta r}$. In Fig. 5 we test this prediction (horizontal solid line) against both experiments and simulations. The experimental and numerical values of P_h were acquired over the injection period $|\, l_h - l \,| < 2$ cm to average out noise of the load cell and fluctuations in the numerics. The standard deviation of $\bar{P}_h$ over this range is represented by the error bars in Fig. 5, and is large in the numerical simulations, presumably, due to a lack of material damping. Elastic waves travel along the rod when it loses contact with the cylindrical constraint to form a helix, which in turn increases the variation in reaction force at the injector. Both experiments and simulations (within considerable uncertainties) exhibit a relatively constant level of $\bar{P}_h$, as expected from Eq. (22), with simulation results consistently above experimental values by $\sim 77\%$. Once again, the agreement between Eq. (22) (without the inclusion of the amplification factor, ψ_c^h) and both the experimental and simulation data was unexpected but supports the appropriateness of the underlying assumptions and the simplicity of our approach.

We have also explored the effect of dimensionless injection speed, $\eta = v/v_{\text{sound}}$ on helical initiation, for two different values of the radial clearance, $\Delta r = 4.42$ and 9.27 mm ($D = 12.0$ and 21.7 mm). This test was essential to check that the experimental apparatus did not induce additional frictional effects due to the buildup of electrostatic charge on the constraining pipe (McCourt et al., 2004). In dimensional terms, the injection speed was varied in the range $1 < v\,[\text{cm/s}] < 20$. In Fig. 6, we find that $\bar{l}_h$ is independent of η, for both values of the radial clearance tested, which is indicative of a consistent coefficient of friction throughout the experimental runs. Again, we see good agreement between the experiments and Eq. (21), even if the latter underpredicts the data by $\sim 12\%$ for all injection speeds tested. Similarly to the results of Fig. 4, we attribute this small discrepancy to the fact that the theoretical prediction only includes axial friction and no lateral friction.

5.3. Effect of natural curvature

All experimental and numerical results described so far were obtained for a naturally straight rod. We proceed by investigating the case of injecting a rod with natural (i.e., intrinsic) curvature, κ_n. We are particularly interested in assessing the effect that κ_n has on the lock-up length, l_l, of the injected rod. This line of inquiry is motivated by recent studies involving naturally curved thin elastic rods in geometrically nonlinear configurations (Lazarus et al., 2013; Lazarus et al., 2013; Miller et al., 2014; Jawed et al., 2014) where there is a threshold value for κ_n, below which the rod behaves as if it was naturally straight and above which the mechanical response of the system can be modified both qualitatively and quantitatively. The values of this critical natural curvature are typically dependent on the system. In the context of the current study, buckling of Coiled Tubing inside a cylindrical constraint, κ_n has been predicted to reduce the lock-up length, l_l, (Qiu et al., 1997; Zheng and Sarmad, 2005) but to the best of our knowledge, this result has not been tested experimentally.

In our experiments, we are able to fabricate naturally curved rods (see Section 3.2 for the protocol details), in a way that κ_n can be systematically varied as a control parameter. Above, we focused on the length for helical initiation, l_h, as a measure for horizontal reach. We now choose to quantify the lock-up length, l_l, to allow for a direct comparison for the predictions in Zheng and Sarmad (2005), where it was assumed that the injected naturally curved rod immediately adopts a helical shape.

In Fig. 7, we plot the dimensionless lock-up length, $\bar{l}_l = l_l/\lambda$, as a function of the dimensionless natural curvature, $\bar{\kappa}_n = \kappa_n \lambda$, obtained from both experiments and simulations. The rod was injected at $v = 0.1$ m/s into a constraining pipe with $D = 18.5$ mm ($\Delta r = 7.67$ mm). For low values of the natural curvature, $\bar{\kappa}_n \lesssim 1$, $\bar{l}_l$ is approximately constant in both experiments and simulations. By contrast, for $\bar{\kappa}_n \gtrsim 1$ natural curvature significantly reduces the lock-up length. There is good agreement between experiments and simulations, without the systematic offset that was found in the Section 5.2. We believe that this is due to the fact

Please cite this article in press as: Miller, J.T., et al. Buckling-induced lock-up of a slender rod injected into a horizontal cylinder. Int. J. Solids Struct. (2015), http://dx.doi.org/10.1016/j.ijsolstr.2015.07.025

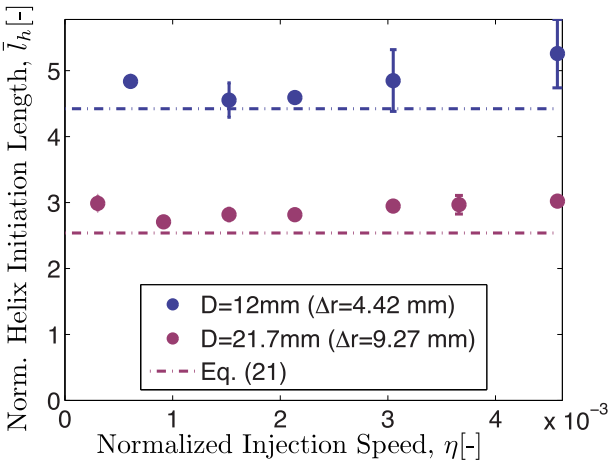

Fig. 6. Experimental values of normalized helical initiation, $\bar{l}_h$, as function of the dimensionless injection speed, η, for $D = 12$ and 21.7 mm ($\Delta r = 4.42$ and 9.27 mm, respectively). Dashed lines correspond to the theoretical prediction in Eq. (21).

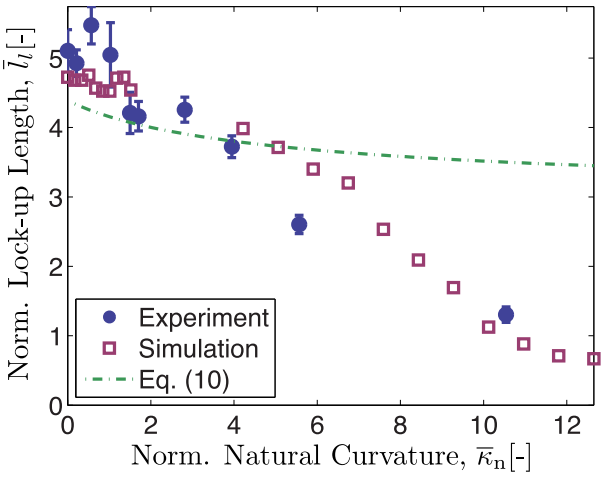

Fig. 7. Normalized lock-up length, $\bar{l}_l$, as a function of normalized natural curvature, $\bar{\kappa}_n$, for experiments (solid points) and simulation (hollow squares) for a constraining pipe $D = 18.5$ mm. The dashed line is Eq. (10) proposed by Zheng and Sarmad (2005).

that here, κ_n becomes the dominant geometric imperfection instead of the manufacturing imperfections for the case of a straight rod, which further supports the rationale provided to interpret the discrepancies in Figs. 4 and 5. Interestingly, we find that our results are in disagreement with Eq. (10) that was proposed in Zheng and Sarmad (2005), which predicted an immediate decrease in $\bar{l}_l$ with increasing $\bar{\kappa}_n$ and significantly overpredicts $\bar{l}_l$ for large values of $\bar{\kappa}_n$.

These findings have two important potential implications for industrial applications of Coiled Tubing. Firstly, our results suggest that there is a threshold at $\bar{\kappa}_n \sim \lambda$ (even if this is not sharp), below which improved fabrication or straightening techniques do not yield significant improvements in l_l. This could be used to guide design tolerances for injected Coiled Tubing and the operational setting of the straightener and 'goose neck' in CT rigs (Fig. 1). Secondly, the rapid decrease in l_l for increasing κ_n past this threshold curvature draws attention to this oft-neglected parameter as an area of potential improvement in CT operations, and highlights the possible benefit of more routinely including pipe straighteners on rigs.

5.4. Relevance of our results to the field scale

Thus far, we have performed precision model experiments at the desktop scale and contrasted these results against numerical simulations. Throughout, we tested theoretical predictions with our physical and numerical experiments. The geometric and material properties of our apparatus were not scaled down one-to-one from the field case, but instead were chosen in order to still reproduce the phenomena within the constraints of a laboratory-scale experiment. Exactly scaling the field problem onto the desktop would have been impractical, but having validated the simulations with our own experiments, this is something that can now be probed numerically.

In Eq. (21) above, we provided an expression for $\bar{l}_h$ as a function of μ and $\xi_{\Delta r}$. According to our scaling analysis in Section 4.3, the dimensionless results reported above (*e.g.*, the variation of $\bar{l}_h$ on $\xi_{\Delta r}$) should be unmodified for a wide range of materials and clearances. To test this, we have performed 42 additional simulations in the ranges $0.005 \leqslant \xi_r \leqslant 0.068$ and $0.002 \leqslant \xi_{\Delta r} \leqslant 0.068$. In Fig. 8, we plot these numerical results of $\bar{l}_h$ versus $\xi_{\Delta r}$ (squares) and superpose the previous experimental and simulation results from Fig. 4. From the dimensional analysis (Section 4.3) we expect $\bar{l}_h$ to be a function of $\xi_{\Delta r}$, but independent of ξ_r, such that all the results should collapse onto a single curve provided by Eq. (21). This collapse is indeed observed for the data in Fig. 8, which further supports our scaling analysis and our modeling approach.

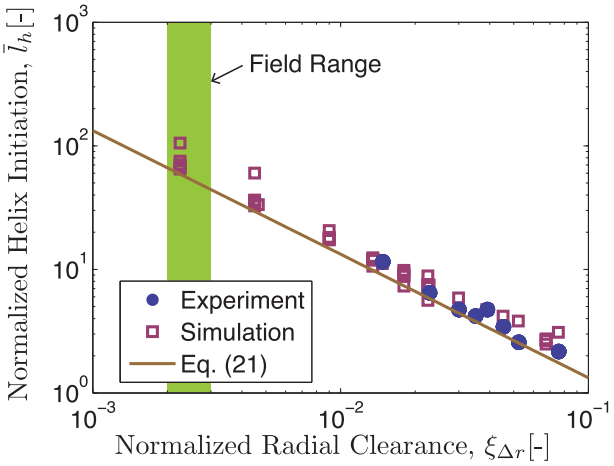

Fig. 8. Results of 8 experimental averages (solid points) and 42 simulations (hollow squares) with different combinations of $(\xi_{\Delta r}, \xi_r)$ parameters. We plot l_h normalized by λ against $\xi_{\Delta r}$, showing small changes in l_h/λ despite changing ξ_r over the range of $0.005 \leqslant \xi_r \leqslant 0.068$ in simulations. This agrees with our scaling analysis of Section 4.3 which concluded that $\bar{l}_h = f(\xi_{\Delta r})$, with no dependence on ξ_r.

We recall that in our experimental data, the dimensionless radial clearance lies in the range $0.015 \leqslant \xi_{\Delta r} \leqslant 0.076$, whereas in the field this parameter lies within $0.002 \lesssim \xi_{\Delta r} \lesssim 0.003$ (shaded region in Fig. 8). On the other hand, the simulations presented in Fig. 8 vary across $0.002 \leqslant \xi_{\Delta r} \leqslant 0.076$, which includes both the field and laboratory cases. Given that excellent agreement is found with Eq. (21), throughout, we conclude that what we have learned through the laboratory experiments is directly relevant to the field scale.

We have focused on the initiation of helical buckling in both experiments and numerical simulations, except in the study of the effect of κ_n, where lock-up was also considered. This was done in order to maintain as much material independence in our results as possible, in particular with regard to plasticity. In the first study that analyzed the helical buckling of tubular structures within a

Please cite this article in press as: Miller, J.T., et al. Buckling-induced lock-up of a slender rod injected into a horizontal cylinder. Int. J. Solids Struct. (2015), http://dx.doi.org/10.1016/j.ijsolstr.2015.07.025

cylindrical constraint, Lubinski and Althouse (1962) derived and discussed an equation for the force needed to plastically deform a helically buckled pipe, which is reproduced here for convenience (with notation altered to be consistent with this paper):

$$\sigma_0 = \frac{P_{h+}}{A} + \frac{OD\Delta r P_{h+}}{4I}, \tag{23}$$

where σ_0 is the stress along the outer fiber of the tubing (which is the region of maximum stress when the Coiled Tubing does not have a pressure differential between its inner diameter and borehole annulus), and other terms have been previously defined. The first term of Eq. (23) corresponds to the axial stress from the applied load and the second term is the bending stress associated with a helical shape (with a pitch length defined by P_{h+} and helical radius Δr).

If we consider $P_{h+} = P_h = 2\sqrt{2}\sqrt{\frac{EIw}{\Delta r}}$ to be an estimate for the axial load for Coiled Tubing in a horizontal wellbore (discussed in Section 5.2), we can estimate the maximum stress in the Coiled Tubing at the onset of helical buckling using typical material properties and geometries of the oilfield (taken from Wicks et al., 2008). We consider Coiled Tubing fabricated with a low-alloy carbon steel with $OD = 0.14$ m, $ID = 0.222$ m, $\Delta r = 0.041$ m, $I = 9.97 \times 10^{-6}$ m^4, $A = 0.0048$ m^2, $E = 207$ GPa, and $w = 315$ N/m, giving P_h=356.2 kN, or $\sigma_0 = 125$ MPa (corresponding to a maximum strain of $\epsilon = 0.06\%$). This stress is well below the yield strength for steel used in Coiled Tubing, which is typically specified to be in the range $379 < \sigma_y\,[\text{MPa}] < 620$ MPa (API, 1996), meaning that the material remains linear elastic up to the initiation of helical buckling.

6. Conclusions

In summary, inspired by Coiled Tubing operations in the oil and gas industry, we have developed a scaled model system to explore the mechanical behavior of a rod injected into a horizontal cylindrical constraint, in the elastic regime, prior to plasticity effects becoming important. Our efforts were centered on helical buckling, with a focus on describing the total length of rod, l_h, that can be injected into the horizontal constraint prior to helix initiation. Helix initiation was chosen as a comparison due to the elastic nature of the buckling process up to that point, even in the field case. The investigation combined experimental, numerical, and analytical approaches. The experimental results were found to be in good agreement with existing theories, in particular regarding the dependence of l_h on radial clearance, despite the *ad hoc* nature of the application of these theoretical predictions. We have also demonstrated that the natural curvature of the rod can have a strong effect on the lock-up length, past a critical value that is yet to be fully rationalized.

The experimental results were also reproduced through detailed computer simulations that involved no fitting parameters. These simulations solved the dynamic Kirchhoff rod equations that took into account twisting, bending, stretching, and shearing of the rod and a careful treatment of the frictional contact between the injected rod and cylindrical constraint.

Good agreement was found between simulations and experiments, which indicated that the analytical model and the underlying simplifying assumptions captured the essential ingredients of the problem. A scaling analysis based on our dimensional dynamic equations identified six dimensionless parameters that characterize the system. Furthermore, the dimensionless parameter $\xi_{\Delta r} = \Delta r/\lambda$, which compares the radial clearance with the buckling wavelength, was identified as key to scaling the buckling geometry from the field case to the desktop.

Future work should test how the proposed scaling analysis for the field data compares with experiments and simulations. Moreover, although this paper has addressed characterizing the lock-up process, we hope that a similar approach may help rationalize recent experiments (Miller et al., 2015) in which vibration was used to destabilize frictional contacts and delay lock-up. This suggests opportunities for substantial gains in reach in horizontal wellbores, which is of timely importance for the oil and gas industry.

Acknowledgments

We are grateful for financial support from both Schlumberger and the National Science Foundation (CMMI-1129894).

References

Acock, A., O'Rourke, T., Shirmboh, D., Alexander, J., Andersen, G., Kaneko, T., Venkitaraman, A., López-de Cárdenas, J., Nishi, M., Numasawa, M., 2004. Practical approaches to sand management. Oilfield Rev., 10–27

Afghoul, A., Amaravadi, S., Boumali, A., Calmeto, J., Lima, J., Lovell, J., Tinkham, S., Zemlak, K., Staal, T., 1994. Coiled tubing: the next generation. Oilfield Rev. 6 (4), 9–23.

Al-Dhufairi, M., Al-Ghamdi, S., Noya, J., Al-Aradi, K., Al-Sarakbi, S., Al-Dossary, A., Krueger, E., Moore, N. 2010. Expanding the envelope of coiled-tubing reach for stimulation of ultradeep openhole horizontal wells. In: SPE/ICoTA Coiled Tubing and Well Intervention Conference and Exhibition, pp. 327–337.

Antman, S.S., 2005. Nonlinear Problems of Elasticity, vol. 107. Springer.

API, 1996. Rp 5c7, Recommended Practice for Coiled Tubing Operations in Oil and Gas Well Services.

Audoly, B., Pomeau, Y., 2010. Elasticity and Geometry: From Hair Curls to the Nonlinear Response of Shells. Oxford University Press, Oxford and New York.

Bennetzen, B., Fuller, J., Isevcan, E., Krepp, T., Meehan, R., Mohammed, N., Poupeau, J.-F., Sonowal, K., 2010. Extended-reach wells. Oilfield Rev. 22 (3), 4–15.

Bhalla, K., 1994. Implementing residual bend in a tubing forces model. In: SPE Annual Technical Conference and Exhibition, pp. 97–112.

Bhalla, K., 1995. Coiled tubing extended reach technology. In: Offshore Europe conference, pp. 392–405.

Brazier, L., 1927. On the flexure of thin cylindrical shells and other thin sections. P.R. Soc. Lon. Ser. A 773, 104–114.

Brusco, G., Lewis, P., Williams, M., 2004. Drilling straight down. Oilfield Rev. 16 (3), 14–17.

Buckingham, E., 1914. On physically similar systems; illustrations of the use of dimensional equations. Phys. Rev. 4 (4), 345–376.

Chen, Y., Lin, Y., Cheatham, J., 1990. Tubing and casing buckling in horizontal wells (includes associated papers 21257 and 21308). J. Petrol. Technol. 42 (2), 140–141.

A. Clebsch, 1862. Theorie der elasticitat fester korper, BG Teubner.

G.W.P. Council, Modern shale gas development in the United States: A primer, US Department of Energy, Office of Fossil Energy, 2009.

Dawson, R., Paslay, P., 1984. Drill pipe buckling in inclined holes. J. Petrol. Technol. 36 (10), 1734–1738.

Deli, G., Liu, F., Xu, B. 1998. An analysis of helical buckling of long tubulars in horizontal wells. In: SPE International Oil and Gas Conference and Exhibition in China, pp. 517–523.

Gao, G., Miska, S., 2009. Effects of boundary conditions and friction on static buckling of pipe in a horizontal well. SPE J. 14 (4), 782–796.

Gao, G., Miska, S., 2010. Effects of friction on post-buckling behavior and axial load transfer in a horizontal well. SPE J. 15 (4), 1104–1118.

Gere, J., 2006. Mechanics of Materials, sixth ed. Cengage Learning.

Goriely, A., Tabor, M., 1998. Spontaneous helix hand reversal and tendril perversion in climbing plants. Phys. Rev. Lett. 80 (7), 1564–1567.

Goyal, S., Perkins, N., Lee, C.L., 2008. Non-linear dynamic intertwining of rods with self-contact. Int. J. Nonlin. Mech. 43 (1), 65–73.

Gupta, V.P., Yeap, A.H., Mathis, R.S., Fischer, K.M., Egan, M.J., et al., 2014. Expanding the extended reach envelope at Chayvo field Sakhalin Island. In: IADC/SPE Drilling Conference and Exhibition, Society of Petroleum Engineers, pp. 1207–1229.

Hughes, B., 2014. Rig count overview and summary count (November 2014) [cited November 2014]. URL <http://phx.corporate-ir.net/phoenix.zhtml?c=79687&p=irol-rigcountsoverview>.

ICoTA, 2005. An Introduction to Coiled Tubing: History, Applications, and Benefits, International Coiled Tubing Association.

Jawed, M.K., Da, F., Joo, J., Grinspun, E., Reis, P.M., 2014. Coiling of elastic rods on rigid substrates. Proc. Natl. Acad. Sci. USA 111 (41), 14663–14668.

Kirchhoff, G., 1859. über das gleichgewicht und die bewegung eines unendlich dünnen elastischen stabes. Journal für die Reine und Angewandte Mathematik 56, 285–313.

Lazarus, A., Miller, J.T., Reis, P.M., 2013. Continuation of equilibria and stability of slender elastic rods using an asymptotic numerical method. J. Mech. Phys. Solids 61 (8), 1712.

Lazarus, A., Miller, J.T., Metlitz, M., Reis, P.M., 2013. Contorting a heavy and naturally curved elastic rod. Soft Matter 9 (34), 8274–8281.
Love, A., 1892. A Treatise on the Mathematical Theory of Elasticity, first ed. Cambridge University Press.
Lubinski, A., 1950. A study of the buckling of rotary drilling strings. Drill. Prod. Pract., 178–214
Lubinski, A., Althouse, W., 1962. Helical buckling of tubing sealed in packers. J. Petrol. Technol. 14 (6), 655–670.
Maddocks, J.H., 1984. Stability of nonlinearly elastic rods. Arch. Ration. Mech. An. 85 (4), 311–354.
MakerBot. Makerbot stepstruder mk4 [online, cited 10/17/2013]. URL <http://www.thingiverse.com/thing:964>.
McCourt, I., Truslove, T., Kubie, J., 2002. Penetration of tubulars into horizontal oil wells. Proc. Inst. Meh. Eng. C - J. Mec. 216 (12), 1237–1245.
McCourt, I., Truslove, T., Kubie, J., 2004. On the penetration of tubular drill pipes in horizontal oil wells. Proc. Inst. Meh. Eng. C - J. Mec. 218 (9), 1063–1081.
Miller, J.T. 2014. Mechanical behavior of elastic rods under constraint (Ph.D. thesis), Massachusetts Institute of Technology.
Miller, J.T., Lazarus, A., Audoly, B., Reis, P.M., 2014. Shapes of a suspended curly hair. Phys. Rev. Lett. 112 (6), 068103.
Miller, J.T., Su, T., Pabon, J., Wicks, N., Bertoldi, K., Reis, P.M., 2015. Buckling of a thin elastic rod inside a horizontal cylindrical constraint. Extreme Mech. Let. 3, 36–44.
Miller, J.T., Mulcahy, C.G., Pabon, J., Wicks, N., Reis, P.M., 2015. Extending the reach of a rod injected into a cylinder through distributed vibration. J. Appl. Mech. 82 (2), 021003.
Miska, S., Cunha, J.C., 1995. An analysis of helical buckling of tubulars subjected to axial and torsional loading in inclined wellbores, in: SPE Production Operations Symposium, pp. 173–180.
Miska, S., Qiu, W., Volk, L., Cunha, J., 1996. An improved analysis of axial force along coiled tubing in inclined/horizontal wellbores. In: International Conference on Horizontal Well Technology, pp. 207–214.
Mitchell, R., 1986. Simple frictional analysis of helical buckling of tubing. SPE Drill. Eng. 1 (6), 457–465.
Mitchell, R., 1997. Effects of well deviation on helical buckling. SPE Drill. Completion 12 (1), 63–70.
Mitchell, R., 2002. Exact analytical solutions for pipe buckling in vertical and horizontal wells. SPEJ 7 (4), 373–390.
Mitchell, R., 2008. Tubing buckling – the state of the art. SPE Drill. Completion 23 (4), 361–370.
Newman, K., Newburn, D., 1991. Coiled-tubing-life modeling. In: SPE Annual Technical Conference and Exhibition, pp. 13–19.
Pabon, J., Wicks, N., Chang, Y., Harmer, R., 2009. Modeling transient vibrations while drilling using a finite rigid body approach. Non-linear Dyn. Deep Drill. Syst. 83.
Pabon, J.A., Wicks, N., Chang, Y., Dow, B., Harmer, R.J., et al., 2010. Modeling transient vibrations while drilling using a finite rigid body approach. In: SPE Deepwater Drilling and Completions Conference, Society of Petroleum Engineers, pp. 293–307.
Pabon, J., Wicks, N., Chang, Y., Chapman, C., Singh, V., 2011. Modeling the transient behavior of BHA/drill string while drilling, U.S. Patent 8014987 (September 2011). Url: <http://www.freepatentsonline.com/8014987.html>.
Palmer, A.C., King, R.A., 2008. Subsea Pipeline Engineering. PennWell Books.
Paslay, P., Bogy, D., 1964. The stability of a circular rod laterally constrained to be in contact with an inclined circular cylinder. J. Appl. Mech. 31, 605–610.
Qiu, W., 1998. Prediction of contact force for drill pipe/coiled tubing. In: SPE Eastern Regional Meeting, pp. 329–342.
Qiu, W., Miska, S., Volk, L., 1997. Effect of coiled tubing (ct) initial configuration on buckling/bending behavior in straight deviated wells. In: Latin American and Caribbean Petroleum Engineering Conference, pp. 1–11.
Roark, R.J., Young, W.C., 1975. Formulas for Stress and Strain. McGraw-Hill.
Shi, Y., Hearst, J., 1994. The Kirchhoff elastic rod, the nonlinear Schrödinger equation, and DNA supercoiling. J. Chem. Phys. 101, 5186.
Timoshenko, S., Gere, J., 1961. Theory of Elasticity Stability,, Dover.
van Adrichem, W., Newman, K., 1993. Validation of coiled-tubing penetration predictions in horizontal wells. J. Petrol. Technol. 45 (2), 155–159.
Wicks, N., Wardle, B., Pafitis, D., 2008. Horizontal cylinder-in-cylinder buckling under compression and torsion: Review and application to composite drill pipe. Int. J. Mech. Sci. 50 (3), 538–549.
Williams, M., 2004. Better turns for rotary steerable drilling. Oilfield Rev. 16 (1), 4–9.
Wu, J., Juvkam-Wold, H., 1993. Study of helical buckling of pipes in horizontal wells. In: SPE Production Operations Symposium, pp. 867–876.
Zheng, A., Sarmad, A., 2005. The penetration of coiled tubing with residual bend in extended-reach wells. In: SPE Annual Technical Conference and Exhibition, pp. 220–225.

Please cite this article in press as: Miller, J.T., et al. Buckling-induced lock-up of a slender rod injected into a horizontal cylinder. Int. J. Solids Struct. (2015), http://dx.doi.org/10.1016/j.ijsolstr.2015.07.025